Anomalous infrasound propagation in a hot stratosphere and the existence of extremely small shadow zones

L. G. Evers,[1,2] A. R. J. van Geyt,[1] P. Smets,[1,2] and J. T. Fricke[1,2]

Received 12 October 2011; revised 16 January 2012; accepted 27 February 2012; published 31 March 2012.

[1] Long-range infrasound propagation strongly depends on the state of the stratosphere. Infrasound can be efficiently ducted between the Earth's surface and the stratopause under a favorable wind and temperature structure between 40 and 50 km altitude. Understanding infrasound propagation under variable stratospheric conditions is of importance for a successful verification of the Comprehensive Nuclear-Test Ban Treaty, in which infrasound is used as a verification technique. Inversely, infrasound observations can be used in acoustic remote sensing of the upper atmosphere. In previous studies, attention has been paid to the strength and direction of the circumpolar vortex wind. In this study, an analysis is made of the temperature effect in the stratosphere on infrasound propagation. A case study is presented from an explosion during a sudden stratospheric warming. During such conditions, the size of the classical stratospheric shadow zone (~200 km) appeared to be reduced by a factor of 2. The occurrence of such conditions is quantified by evaluating 10 years of atmospheric specifications. It unexpectedly appeared that the size of the shadow zone can become smaller than 100 km, which is confirmed by evaluating infrasound detections from mining blasts in southwestern Siberia, Russia. These results are valid over a latitudinal range of 20°N to 60°N, which is determined by the stratospheric surf zone.

Citation: Evers, L. G., A. R. J. van Geyt, P. Smets, and J. T. Fricke (2012), Anomalous infrasound propagation in a hot stratosphere and the existence of extremely small shadow zones, *J. Geophys. Res.*, *117*, D06120, doi:10.1029/2011JD017014.

1. Introduction

[2] Infrasound is used as a verification technique for the Comprehensive Nuclear-Test Ban Treaty (CTBT) which has led to a renaissance of its study since 1996, i.e., the date the treaty opened for signing [*Dahlman et al.*, 2009]. The treaty is verified with the International Monitoring System (IMS), which next to infrasound recordings, also consists of seismic, hydroacoustic and radionuclide measurements. Not only the detection of a specific source is subject of current research, also the ability of infrasound to probe the upper atmosphere starts to be (re)exploited [*Donn and Rind*, 1971; *Le Pichon et al.*, 2010]. It has been noted that the detectability of infrasound strongly depends on the stratospheric winds ($\vec{u}$) and temperature (T), since the effective sound speed ($c_{eff} = 20.05\sqrt{T} + \hat{n}\cdot\vec{u}$) is a function of both atmospheric parameters. Actual observations of upper atmospheric winds and temperatures might contribute to atmospheric models which have a limited resolution at these altitudes.

[3] Seasonal changes in the stratospheric wind direction and strength have been analyzed and translated to an infrasound network detection capability [*Le Pichon et al.*, 2009; *Green and Bowers*, 2010]. The best performance is reached under winter conditions on the Northern Hemisphere with strong westerly stratospheric winds.

[4] Knowledge on the stratospheric wind and temperature conditions is essential for a successful verification of the CTBT. *Che et al.* [2011] have shown how the locations of mining events can be improved by using seasonally dependent traveltime curves, compared with ground truth from seismic data.

[5] Previous studies have also identified very fast acoustic phases under stratospheric winds that reached Mach numbers over 0.5, shedding a new light on infrasound propagation [*Kulichkov et al.*, 2004; *Evers and Haak*, 2007]. As the winds turn, around the equinoxes, but also during sudden stratospheric warmings (SSW), the amplitudes of ambient coherent infrasound noise decrease [*Rind and Donn*, 1978] or infrasound suddenly appears from the opposite direction than expected under regular winter conditions [*Evers and Siegmund*, 2009; *Hedlin et al.*, 2010]. However, less attention has been paid to stratospheric temperature variations, next to the wind.

[6] In this study, the propagation of infrasound through a hot (>20°C) stratosphere is analyzed. The ground truth infrasound data comes from a domestic explosion in Belgium, observed with infrasound arrays in the Netherlands. The size of the classical shadow zone (~200 km [see, e.g., *Gutenberg*, 1939]) for the stratosphere is strongly reduced

[1]Seismology Division, Royal Netherlands Meteorological Institute, De Bilt, Netherlands.
[2]Acoustic Remote Sensing Group, Faculty of Aerospace Engineering, Delft University of Technology, Delft, Netherlands.

0148-0227/12/2011JD017014

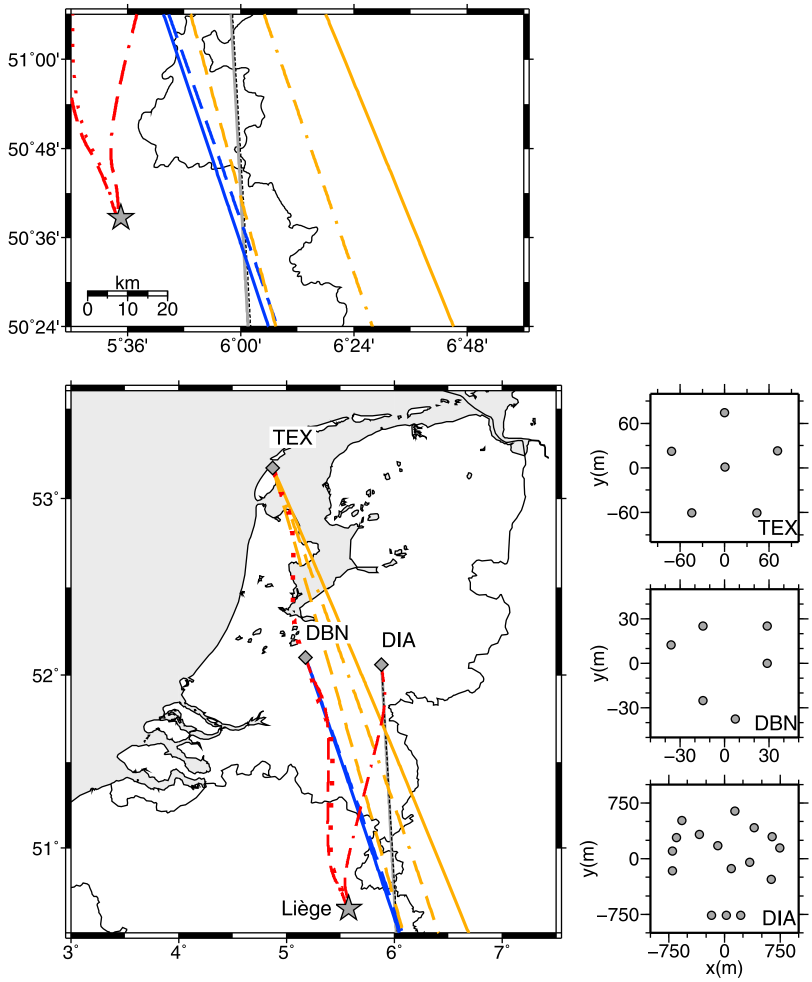

Figure 1. (bottom) (left) Map with the locations of the infrasound arrays in the Netherlands (diamonds) and (right) their layouts. The location of the domestic gas explosion in Belgium, in the city of Liège, is indicated with the gray star. The observed back azimuths from the various arrivals at each array are shown as lines (refer to Table 1 for the exact values). The red curved lines (dash-dotted) are projections of the eigenray trajectories on the surface for rays connecting the source and DIA, DBN and TEX. (top) Magnification of the area around Liège.

under the SSW conditions. How often such conditions occur is evaluated with 10 years of atmospheric specifications. Unexpectedly small shadow zones, of less than 100 km, are predicted by the modeling due to stronger gradients in c_{eff}. To confirm these modeling results, infrasound observations are evaluated from mining blasts in southwestern Siberia, Russia, recorded by the IMS infrasound array I46RU.

2. Infrasonic Data Analysis

[7] Three microbarometer arrays in the Netherlands recorded infrasound from an explosion in Belgium. A domestic gas explosion was reported in the media that took place in early morning of 27 January 2010, around 01:00 UTC. The location was estimated at 50.644°N, 5.576°E, by combining footage in the media with Google Earth (see, for example, http://news.bbc.co.uk/2/hi/europe/8482621.stm). The infrasound arrays in the Netherlands consist of in-house developed microbarometers capable of measuring infrasound in the frequency of 0.002 to 20 Hz, being sensitive in the millipascals to several tens of pascals range [*Mentink and Evers*, 2011]. As can been seen in Figure 1, the array layouts vary in number of elements from 6 to 16; the apertures are in the range of 75 to 1500 m.

[8] Detection of coherent signals is done on the basis of evaluating the Fisher ratio (F) of the variances in the infrasound recordings. F is related to the signal-to-noise ratio (SNR) as $F = 1 + N \cdot \mathrm{SNR}^2$, with N being the number of microbarometers in the array [*Melton and Bailey*, 1957]. As a next step, the slowness as an event characteristic parameter is estimated. Slowness ($\vec{p}$) is then translated to back azimuth (ϕ) and apparent sound speed (c_{app}). The latter being a measure of the incidence angle of the infrasonic wave on the array [see, e.g., *Evers and Haak*, 2007].

[9] Figure 2 gives the results of the above described analysis, where F is calculated over 10,000 beams, or a 100×100 $\vec{p}$ grid. The windowing in time is 3.2 s for the small arrays (DBN and TEX) and 6.4 s for the larger DIA array. All processing is done with Butterworth band-pass-filtered data from 2 to 8 Hz with time windows that overlap 10%. The results of this processing approach can be

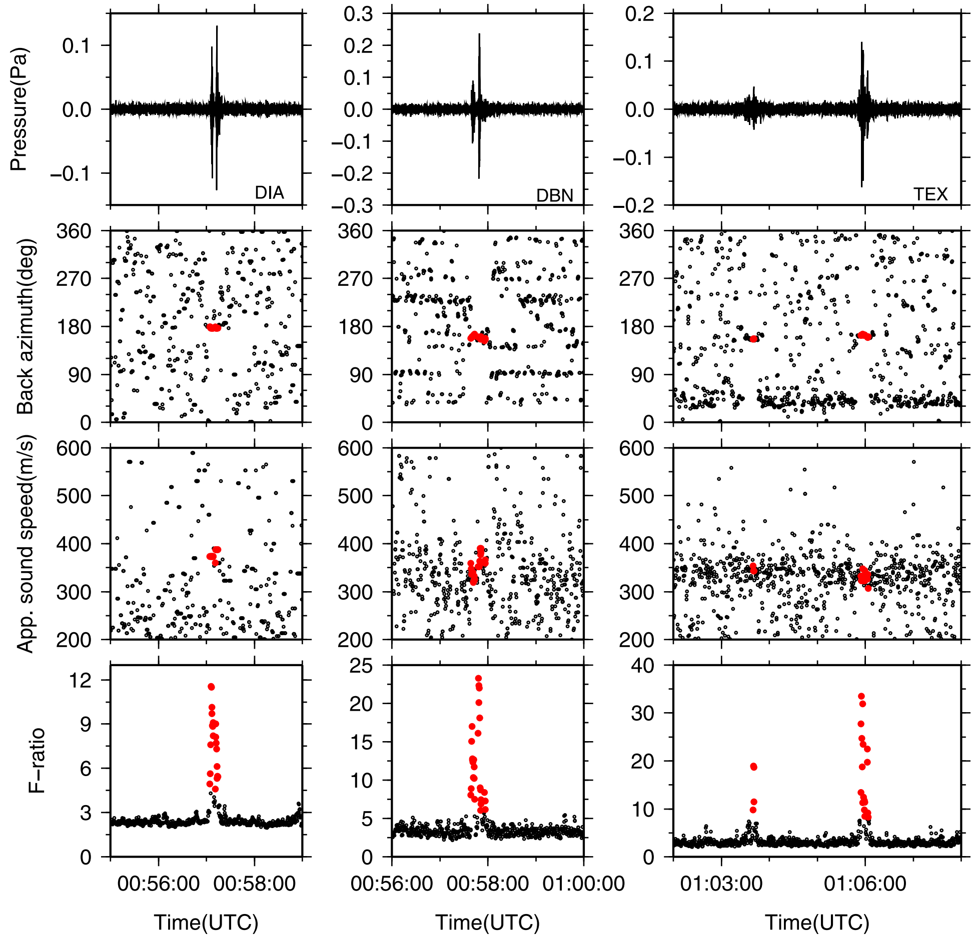

Figure 2. Processing results from the (left) DIA, (middle) DBN and (right) TEX infrasound arrays. From bottom to top, F, apparent sound speed, back azimuth and the best beam are given as function of time on 27 January 2010. Red dots are used to indicate the events. Note that the time scale in TEX is 2 times larger than the ones at the other arrays.

found in Table 1, and the obtained back azimuths are plotted in Figure 1.

[10] All arrays detected a sequence of two impulsive arrivals within a package of coherent energy that lasted approximately ten seconds. In addition, TEX detected a second package of energy in front of the above mentioned sequence. The first impulsive arrival of the observed sequences has a lower azimuthal deviation and lower apparent sound speed than the second one, which is consistent over all arrays. From this observation, it can be inferred that the second arrival propagated to higher altitudes than the first one. At such altitudes, the stratospheric cross winds will be stronger which leads to a larger azimuthal deviation. Furthermore, the higher refraction altitude can explain the higher apparent sound speed or steeper angle of incidence [*Evers and Haak*, 2007].

[11] The signal-to-noise ratios are in the range of 0.9 to 2.3 which is quite a large spread indicating that the local noise conditions at the arrays might have varied significantly. Such noise can be caused by wind and turbulence that will alter the signal coherency. Furthermore, the sizes of the arrays differ a lot, especially in the case of DIA with an aperture of 1500 m versus those of the other arrays (75 and

Table 1. Summary of Beam-Forming Results

	Array			
	DIA	DBN	TEX	Phase
Distance (km)	158.9	164.3	285.4	
True back azimuth, ϕ_{true} (deg)	187.8	170.2	170.0	
Arrival time (UTC)	00:57:06.0	00:57:40.5		Is_{35}
	00:57:12.0	00:57:48.5	01:03:40.5	Is_{45}
			01:05:55.3	$IsIs_{35}$
			01:06:02.5	$IsIs_{45}$
SNR	1.0	1.6		Is_{35}
	0.9	1.9	1.7	Is_{45}
			2.3	$IsIs_{35}$
			1.9	$IsIs_{45}$
ϕ_{obs} (deg) ($\Delta\phi$)	176.8 (−11.0)	160.9 (−9.3)		Is_{35}
	176.6 (−11.2)	160.3 (−9.9)	156.5 (−13.5)	Is_{45}
			163.9 (−06.1)	$IsIs_{35}$
			159.8 (−10.2)	$IsIs_{45}$
c_{app} (m/s)	373.0	340.3		Is_{35}
	387.6	351.7	342.7	Is_{45}
			322.5	$IsIs_{35}$
			326.0	$IsIs_{45}$

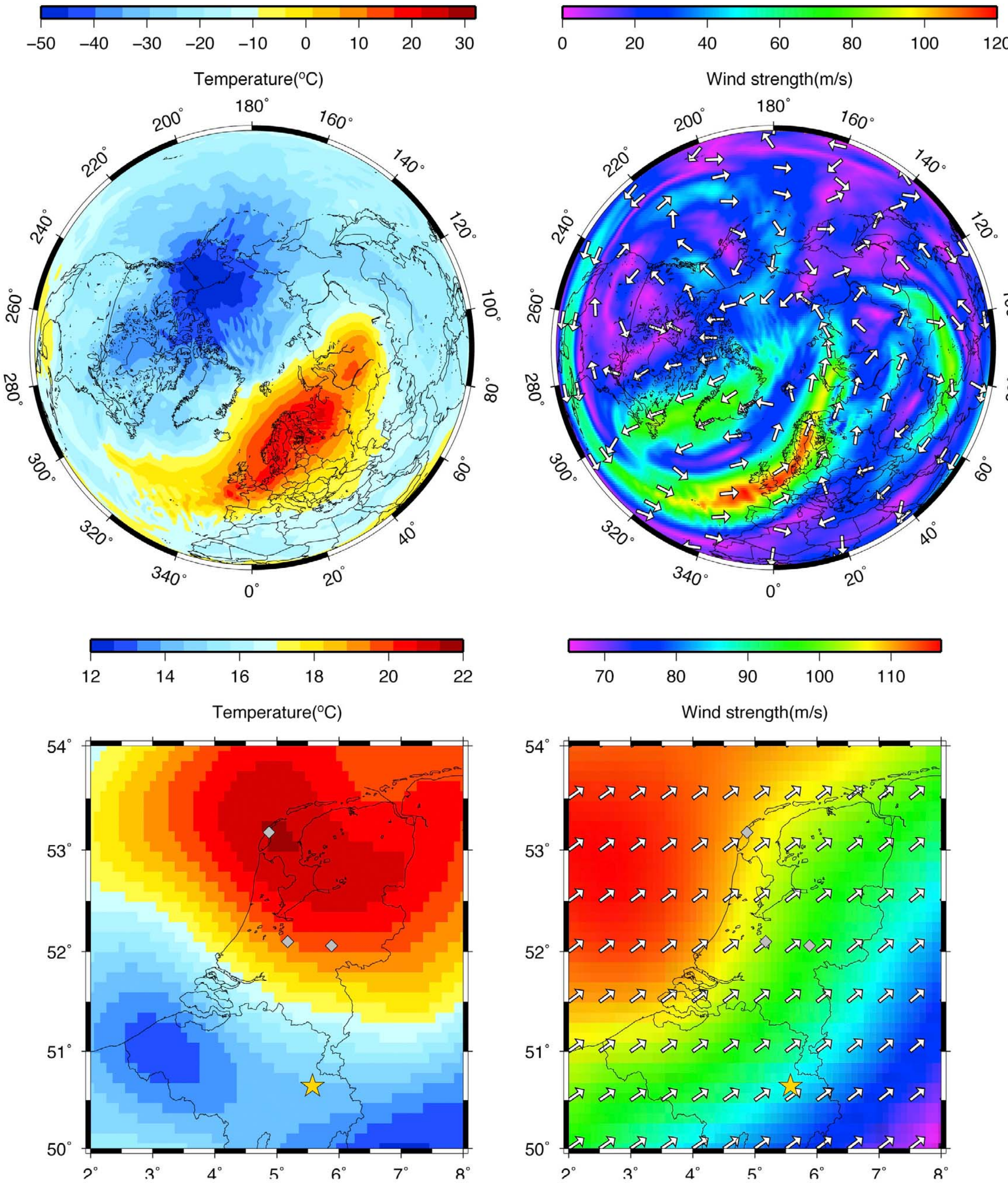

Figure 3. (top left) The temperature and (top right) wind at 50 km altitude from the ECMWF analysis valid for 27 January 2010, 00:00 UTC. (bottom) Zooms of the region of interest (Belgium and Netherlands), with the Dutch arrays as gray diamonds and the explosion location as yellow star.

180 m). The coherency length of the relatively high frequent infrasound (2–8 Hz) could have made DIA less suitable to detect these signals at a high SNR [*Mack and Flinn*, 1971]. In section 3, the propagation of the infrasound through the stratosphere is evaluated, to better understand the signal characteristics at the different arrays, as derived from the array processing.

3. Propagation in the Hot Stratosphere

[12] Figure 3 shows the temperature and wind field at 50 km altitude, derived from the analysis of the European Centre for Medium-Range Weather Forecasts (ECMWF), and valid for 27 January 2010 at 00:00 UTC. The polar vortex wind is clearly distorted from its regular circumpolar flow. The temperature reaches high values of over 30°C above northwestern Europe. Such a state of the stratosphere is associated with a sudden stratospheric warming (SSW) [*Holton*, 2004]. In this case, a SSW occurred in the Northern Hemisphere during January 2010.

[13] From Figure 3 it follows that there is a significant lateral variation in the stratosphere which might influence the propagation. Therefore, the propagation of infrasound is simulated with both one- and three-dimensional atmospheric

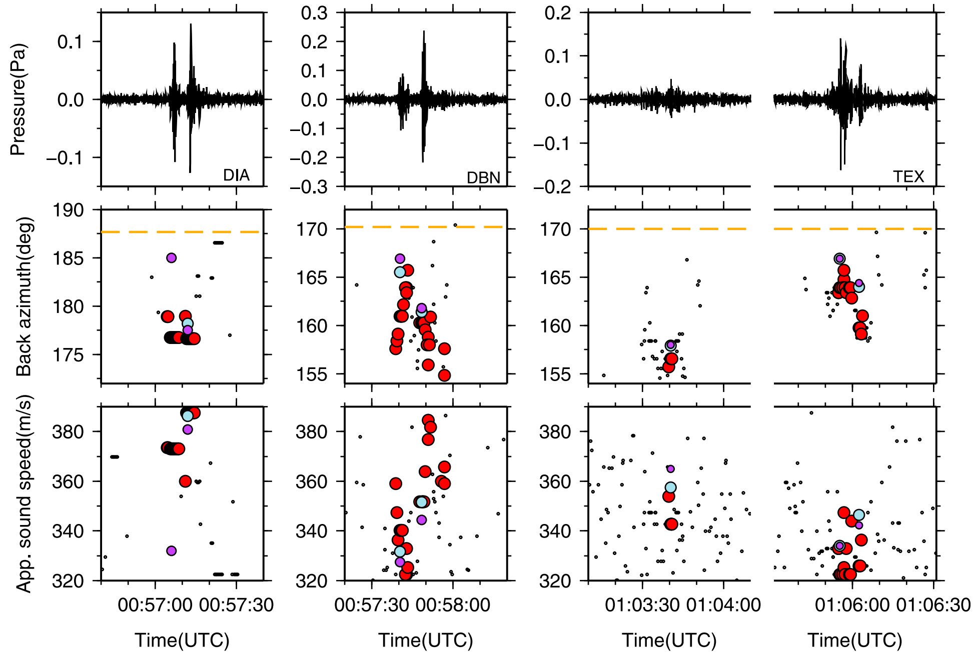

Figure 4. Modeling results for (left) DIA, (middle) DBN and (right) TEX from ray tracing. From bottom to top, the apparent sound speed, back azimuth and the best beam are shown as function of time. Red dots are detections from the Fisher ratio analysis (see Figure 2), blue dots follow from 1-D ray tracing and purple dots from 3-D ray tracing. The orange dashed lines are the true back azimuths. Each window has a length of 1 min; the TEX recording is split into two segments.

profiles, 1-D and 3-D, respectively, with a ray tracer, to assess the influence of the 3-D structure. The ray tracer is based on the Hamilton equations which correspond to the Eikonal equation of the wave equation [see, e.g., *Arnold*, 2004]. The equations were formulated in spherical coordinates and applied in a 3-D atmospheric model. The 3-D wind and temperature profiles were built with third-order splines and 3-D cubics between given ECMWF specifications (0.5° × 0.5°).

[14] The results are given in Figure 4 as colored dots (blue and purple) for the apparent sound speed and the back azimuth. The outcome from the *F* detector as shown in Figure 2 is added as red dots. The results of 1-D and 3-D modeling are in agreement, i.e., small differences between the two, except for DIA. The first arrival in DIA is only generated in the 3-D model.

[15] An example of the ray trajectories for the 3-D case is shown in Figure 5 for paths from the source to DBN and

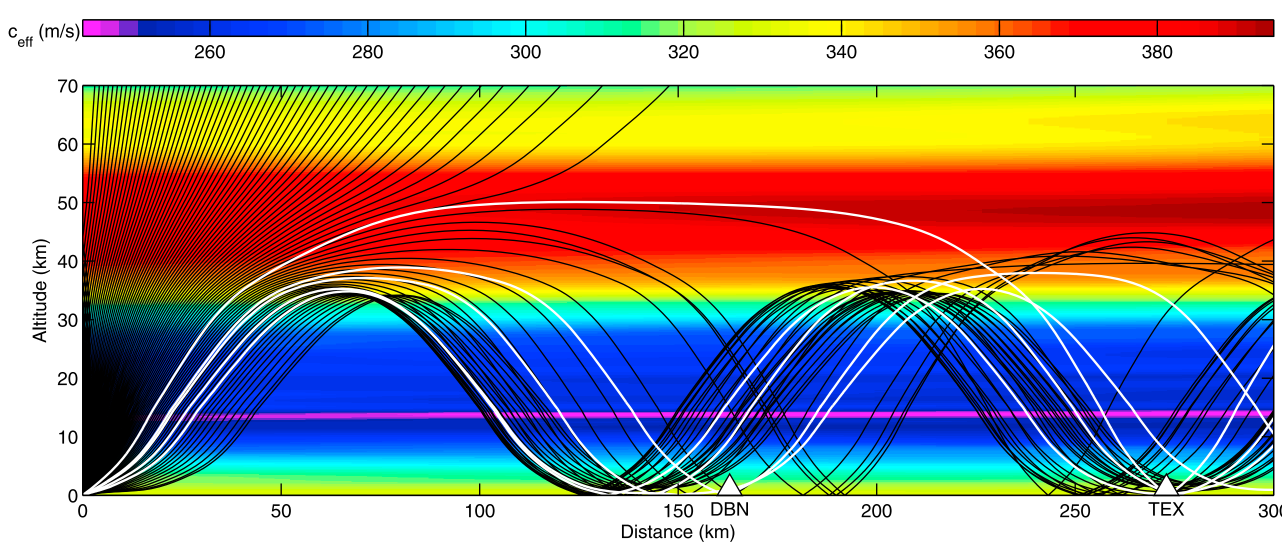

Figure 5. The 3-D ray tracing results for infrasound traveling from Liège to DBN and TEX (white triangles). The effective velocity (c_{eff}) is color coded and derived from the ECMWF analysis. The ray trajectories are plotted in black. The eigenrays, connecting source and receivers, are given as white lines.

TEX which are on a equal azimuth of 350.5°. Refractions from higher altitudes (~45 km) appear with a higher apparent sound speed than those from lower altitudes (~35 km, see also the phases in Table 1). As expected from the array processing results, the higher turning altitudes explain the steeper angle of incidence while the stronger cross winds (~100 m/s) at these altitudes give rise to the larger back azimuthal deviations. It should also be noted that TEX can only just be reached by *IsIs* rays which explains the low observed c_{app} values.

[16] The derived origin times of the explosion are 00:47:41 ± 13.7 and 00:47:40 ± 12.6, resp. for the 1-D and 3-D case. These origin times are based on the modeled traveltimes and averaged over the various phases. The similar absolute values and comparable variances of the origin times again show the minimal difference between 1-D and 3-D modeling over ranges of ~160 to 285 km.

[17] The projections on the surface of the ray trajectories are added to Figure 1 as red dashed and dotted lines for each array. The stratospheric eastward winds translate the rays to east at high altitudes. The skill of the modeling is illustrated by the angle at which the trajectories approach the array. The observed and modeled back azimuths are in agreement.

[18] From the ray trace modeling it follows that the observations are well explained by the combination of 1-D or 3-D propagation and ECMWF models. In other words, the temperature effect in the stratosphere from the ECMWF analysis is confirmed by the infrasound observations and vice verse. In this case, the effective sound speed increase between 35 and 45 due to the warming led to shadow zone sizes down to 110 km. In section 4, it is quantified as to how common such conditions are on the basis of the size of the shadow zone.

4. How Anomalous Are the Conditions of 27 January 2010?

[19] To analyze how often conditions like those on 27 January 2010 occur, the wind and temperature are evaluated at 50 km altitude for 52°N, 5°E from 2001 up to 2010, four times per day (00:00, 06:00, 12:00 and 18:00 UT) from the ECMWF analysis. A period of 10 years is chosen to cover a representative amount of SSWs. Minor SSWs occur every year, while major SSWs occur ones every other year [*Holton*, 2004]. If the temperature around the stratopause is higher than the temperature on the Earth's surface, refraction can occur solely on the basis of the temperature gradient. In general, the temperature around the stratopause ranges between −20°C in winter and 10°C in summer at midlatitudes on the Northern Hemisphere. Rays are propagated through a 1-D model [*Garcés et al.*, 1998] in the direction of the wind at 50 km, doing so, a minimum value for the stratospheric shadow is derived because the steepest gradient in c_{eff} is used. Figure 6 shows the minimum size of the shadow as function of time and the corresponding winds and temperatures at 50 km altitude. Out of the 14,608 models, in 9,076 of the cases stratospheric returns are generated. More returns are observed in winter (black dots) than in summer (gray dots), i.e., 7420 versus 1656, respectively. There is a general trend of large shadow zones in summer and smaller ones in winter, with average sizes of 149 and 239 km, and an overall range of 90 to 400 km. Hardly any returns are observed around the equinoxes because the wind strength is too low. 391 Extremely small shadow zones (3%) of less than 100 km were found of which 101 had higher temperatures around 50 km than at the Earth's surface. The latter means that 1% of the time, stratospheric returns can be expected solely on the basis of the temperature gradient. Shadow zones of less than 100 km are generated with an additional wind component and occur 2% of the time. A summary of the modeling results can be found in Table 2.

[20] The above results are valid for 52°N, 5°E but the polar vortex extends over a broad latitudinal range. The question arises over what range the results can be expected to be applicable? *McIntyre and Palmer* [1984] proposed the so-called stratospheric surf zone where the main polar vortex is surrounded by edges in which a high degree of mixing occurs due to breaking of planetary waves. *Plumb* [1996] extended this model with the existence of a tropical pipe, i.e., an area of upward movement of stratospheric air surrounding the equator. This air can enter the surf zone after which downward movement occurs toward the polar latitudes, conform the Brewer-Dobson circulation [*Holton*, 2004]. On the basis of the above studies, the stratospheric surf zone is determined as the area between 20°N (20°S) and 60°N (60°S).

[21] Unexpectedly, it was found in the above modeling approach that stratospheric shadow zones can become very small, i.e., less than 100 km, within the stratospheric surf zone from 20°N to 60°N. In section 5, we explored whether there is also observational evidence for these findings.

5. Observational Proof of Extremely Small Shadow Zones

[22] In order to find suitable settings for small shadow zones, the Reviewed Event Bulletin (REB) from the International Data Center (IDC) from the CTBTO was investigated (D. Green, AWE Blacknest, United Kingdom, personal communication, 2010). The REB contains, among others, locations and origin times from events detected with the waveform technologies of the IMS: seismic, hydroacoustic and infrasonic. Source locations in southwestern Siberia, Russia, in the vicinity of the IMS infrasound array I46RU appeared to be a likely candidate. Figure 7 shows the location of I46RU, its layout and the events that appeared in the REB (red dots, for a distance less than 110 km and in the back azimuthal range of 59.5° to 90.5°, and blue dots for all other locations). The event locations are seismically determined with IMS seismic arrays in Russia: Zalesovo (53.95°N, 84.82°E), and in Kazakhstan: Kurchatov (50.62°N, 78.53°E), Borovoye (53.02°N, 70.39°E) and Makanchi (46.79°N, 82.29°E). At least two of the seismic arrays have contributed to the locations and origin times of the events. Figure 7 also shows the magnitude distribution of the events. There are 586 blue events within the local magnitude (M_l) range of 1.5 to 4.0 and there are 168 red events in the range of M_l 2.1 to 3.6. The errors in the locations are in the order of a couple of kilometers. All chosen events have an associated infrasound signal at I46RU which makes open pit mining a likely source in this low-seismicity area.

[23] In Figure 8, the distances of the events to I46RU are given as a function of time in Figure 8 (fifth panel), following the coloring coding from Figure 7. The apparent

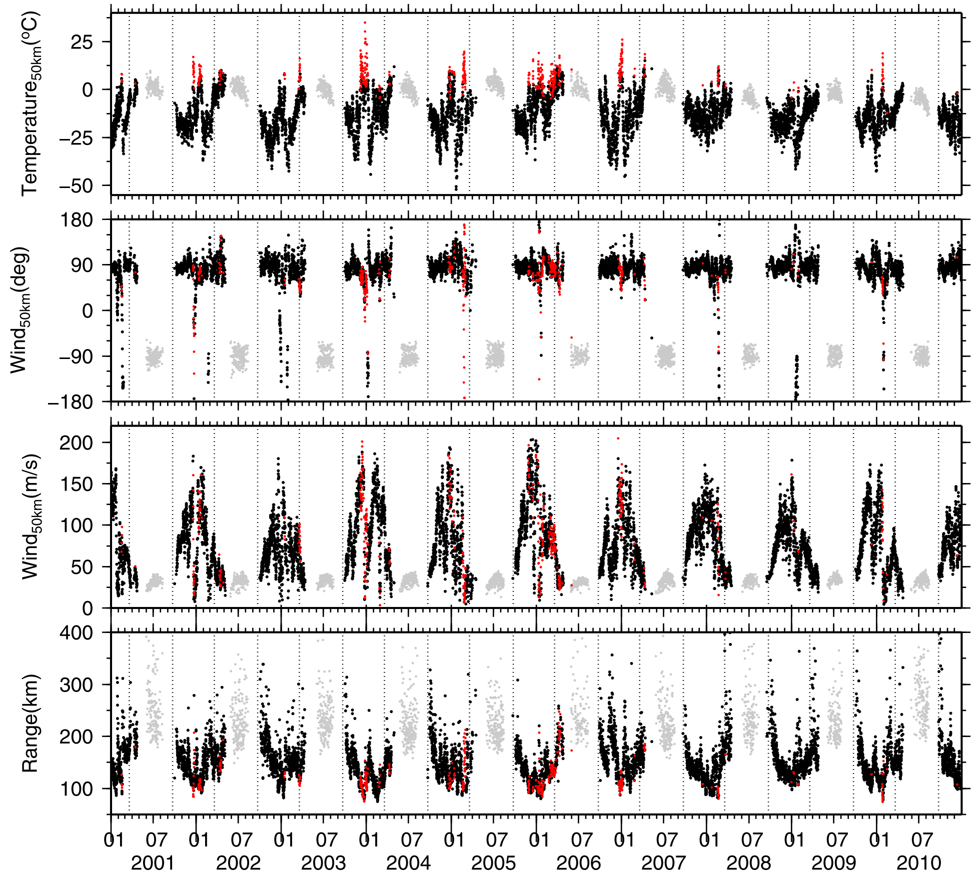

Figure 6. (fourth panel) The minimum size of the stratospheric shadow as function of time from ECMWF atmospheric specification for 52°N, 5°E. The equinoxes are given as dotted vertical lines. The red dots are used when a positive difference occurs between the temperature at 50 km altitude and the Earth's surface. Gray dots are for summer, i.e., between the March and September equinoxes, black dots for winter. Subsequently shown are (third panel) the wind strength at 50 km altitude, (second panel) the corresponding wind direction (90° for eastward and −90° for a westward wind) and (first panel) the temperature at 50 km altitude.

sound speed, c_{app}, of the associated infrasound detections at I46RU are given in Figure 8 (fourth panel). Additionally, all events in the range of 59.5° to 90.5° are added as gray dots to confirm the trend. From the latter, no distance information is available since single detections at an infrasound array cannot provide such information from distant sources.

[24] The question now arises: what is the origin of these detections, characterized by c_{app}, at I46RU? Are these stratospheric refractions or tropospheric arrivals? The structure of the arrival's c_{app} is indicative for stratospheric refractions, i.e., refractions benefiting from the increased temperature in the ozone layer and a possible downwind component. The reasoning is as follows: (1) during the equinoxes hardly any detections are made and (2) during winter conditions, summer-like apparent velocities appear which could only be caused by SSWs. Stratospheric conditions of wind and temperature correspond to the number of detections at I46RU and consequently to the variation in c_{app}.

[25] To further interpret the detections at I46RU, the differences in c_{eff} at a certain altitude and the value at the surface are added to Figure 8. A positive difference, of this Δc_{eff}, means that refraction can occur from that altitude back to the Earth's surface. ECMWF atmospheric specifications at 54.0°N, 85.5°E are chosen to calculate Δc_{eff}, which is in between the mines and I46RU. An azimuth of 254.5° is used from the source region toward I46RU. The results of these calculations are shown in Figure 8 (third panel). The westward circumpolar vortex in summer clearly results in a positive Δc_{eff}. In other words, stratospheric refractions from the mining blasts are likely to be observed at I46RU during summer. But also during winter, a large portion of the time Δc_{eff} is positive although the polar vortex is expected to be predominantly eastward. It appears that SSWs are responsible for this reversed picture and will enable stratospheric

Table 2. Summary of Modeling Results

	Number	Percentage
Models	14608	100%
Shadow zone	9076	62%
Winter	7420	51% (82%)
Summer	1656	11% (18%)
Shadow zone <100 km	392	3%
$\Delta T <= 0$°C	291	2% (74%)
$\Delta T > 0$°C	101	1% (26%)

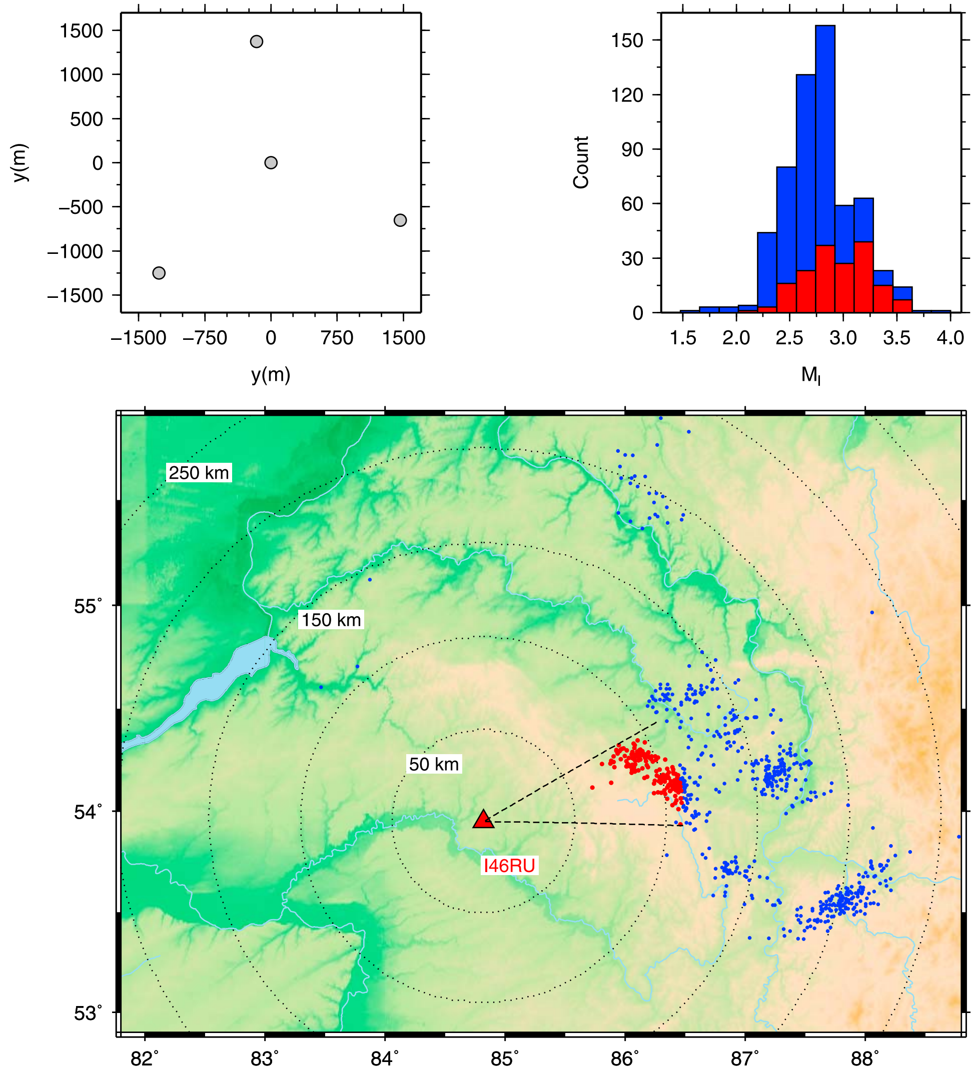

Figure 7. (bottom) Map showing the location of IMS array I46RU in southwestern Siberia, Russia. The red and blue dots are seismic locations from the REB assumingly related to mining activity, i.e., blasting. Mines at a distance of less than 110 km are denoted by red dots within the back azimuthal interval between 59.5° and 90.5°, indicated by the dashed lines. The black dotted circles indicate the distances to I46RU in 50 km intervals. (top) (left) The layout of I46RU and (right) the magnitude (M_l) distribution of the events.

refractions to be recorded during winter. No stratospheric refractions are expected during the equinoxes due to the lack of a downwind component and moderate stratospheric temperatures.

[26] Figure 8 (second panel) shows a cross section through Δc_{eff} at an altitude of 40, 50 and 60 km. The curves are somewhat smoothed by a polynomial fit to aid the interpretation. It follows that, the altitude at which rays bend back to the surface differs from season to season and also within the seasons. The warming of January 2010 leads to a rather high altitude of bending at its starts, of 50 to 60 km. As the warming matures during February, it sinks into the lower stratosphere leading to lower altitudes of bending, around 40 km. The warming of January 2011 is smaller in size and leads to rather constant and low bending altitudes of around 40 km. In summer, most of the time bending altitudes of 50 to 60 km are predicted.

[27] The temperature difference between 50 km altitude and the surface is plotted in Figure 8 (first panel). Clearly, periods of high temperatures exist in the stratosphere during winter which are associated to SSWs. Especially, during the warming of January 2010 there is a two week period with very high stratospheric temperatures that contributed to a positive Δc_{eff} as seen during the explosion in Liège (see Figure 3).

[28] The remaining question to be solved is: why is c_{app} in winter, in general, smaller than in summer? To answer this question, two issues should be considered: (1) the surface temperature and (2) the gradient of c_{eff} as function of altitude in the stratosphere. The sound speed (c_T) is added to Figure 8 (fourth panel) and calculated from the surface temperature from the ECMWF specifications. As expected, the c_T increases in summer due to the higher surface temperature. Consequently, c_{app} will follow the same trend which is clear from comparing the observations of c_{app} with the c_T values.

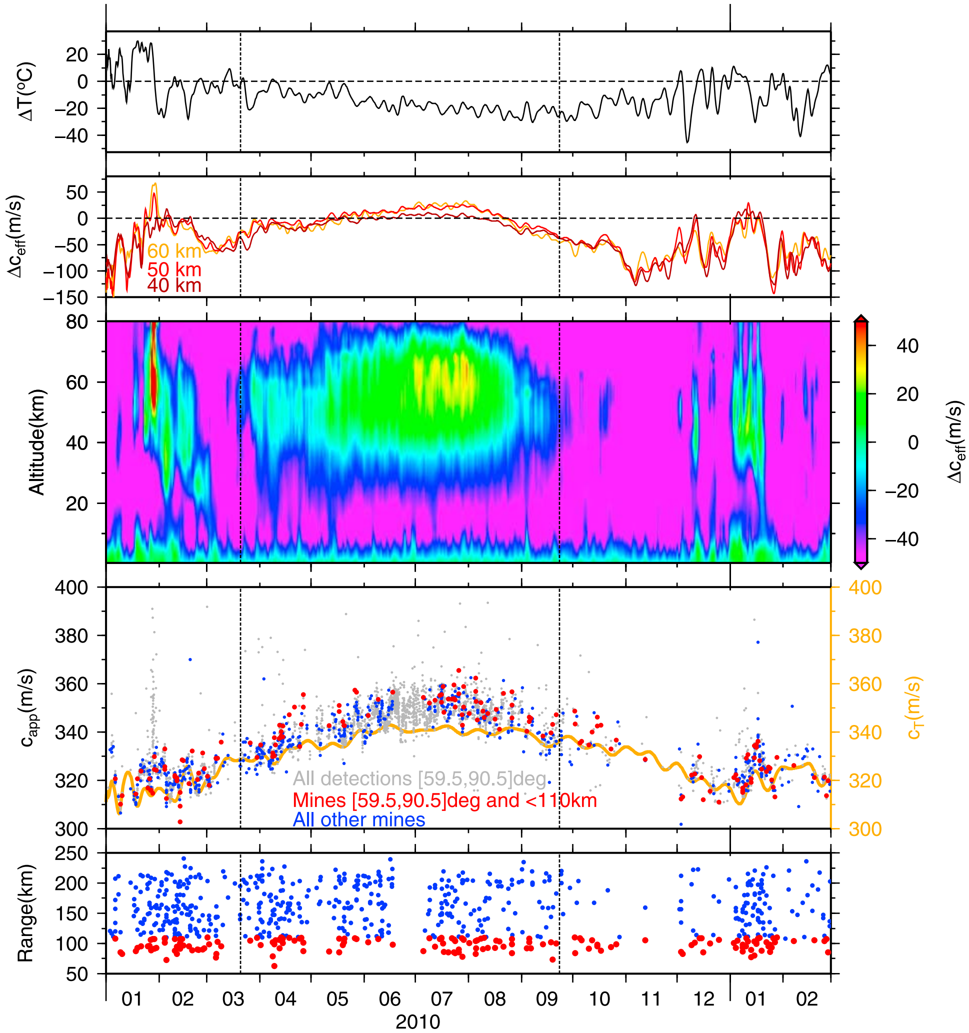

Figure 8. Detections made at I46RU and atmospheric specifications. (fifth panel) The distances of the sources with respect to I46RU as function of time. The color coding is similar to Figure 7. (fourth panel) The apparent sound speed, c_{app}, of the detections, all other detections within 59.5° to 90.5° are added as gray dots. The surface sound speed c_T is given as orange line and calculated from the temperature. (third panel) The difference between the effective sound speed at a certain altitude and near the surface, color coded as Δc_{eff}. The latter are derived from ECMWF specifications at 54.0°N, 85.5°E. (second panel) Cross sections from Δc_{eff} at an altitude of 40, 50 and 60 km. (first panel) The temperature difference between 50 km altitude and the surface, ΔT. The c_T, Δc_{eff} and ΔT curves are smoothed with a polynomial fit.

An additional effect follows from the difference in the gradient of c_{eff} between winter and summer. The winter polar vortex is stronger and has its maximum at a lower altitude than the summer vortex. The resulting stronger gradient, leads to a lower refraction altitude in winter than in summer. Thus, c_{app} in winter is lower than in summer. This effect additional can also be seen in Figure 8 (fourth panel) since the difference between the observations (dots) and c_T are larger in summer than in winter. The steepness of the gradients are also visible in Figure 8 (third panel). In winter there is a faster change from negative to positive Δc_{eff} values than in summer. Small blue colored bands in winter versus broad bands in summer are representative for this difference in the gradient.

[29] In general, the observations and the modeling results are in agreement and the existence of extremely small shadow zones is validated with observations at I46RU.

6. Discussion and Conclusions

[30] In this study, infrasound propagation through a hot stratosphere was analyzed for midlatitudes on the Northern Hemisphere. A case study was presented of a domestic gas explosion in Belgium observed with infrasound arrays in the Netherlands. The combined effect of wind and temperature (>20°C) around the stratopause led to a very small shadow zone for stratospheric refractions of 110 km and was related to a SSW.

[31] Ten years of ECMWF atmospheric specifications have been analyzed in order to quantify the size of the shadow zone. Stratospheric returns occurred 62% of the time and mostly in winter (51%). Hardly any returns are observed around the equinoxes due to the lack of significant downwind component at 50 km altitude. Very small shadow zones of less than 100 km occurred 3% of the time. In some of such cases, the temperature around the stratopause is higher than the temperature at the Earth's surface and mostly associated with SSWs (1% of the time), during such times no additional downwind component is necessary to enable refraction back to the Earth's surface.

[32] Infrasound from mining blasts in southwestern Siberia, Russia, confirm the existence of small shadow zones. However, it should be noted that more stratospheric arrivals are observed than predicted by the modeling. Fine-scale structure in the wind and temperature, which is not resolved by the ECMWF models, and caused by internal gravity waves is responsible for generating additional arrivals [*Kulichkov et al.*, 2010; *ReVelle*, 2010; *Chunchuzov et al.*, 2011]. Although, it is beyond the scope of this paper to model each arrival individually, I46RU provides an interesting data set to apply Kulichkov's theory as has been done by, for example, *Green et al.* [2011] in explaining unexpected arrivals. A full-wave model rather than ray tracing might even predict smaller shadow zones, with a stratosphere containing fine-scale structure. Such modeling would allow for scattering and diffractions and can more accurately predict the size of the shadow zone.

[33] In connection to the above, some of the observations lay below the c_T curve which is physically impossible (see Figure 8, fourth panel). The sound speed is the lowest possible value for the propagation velocity, both for c_{app} and c_{eff}. The fact that lower values of c_{app} exist should be attributed to uncertainties in the traveltime observations and the derived c_{app} with array processing. Another uncertainty comes from the surface temperature, which forms the basis for c_T. The temperature is taken from ECMWF specifications and is not an actual measurement at the station.

[34] Nevertheless, the general trend of stratospheric variations, i.e., summer versus winter characteristics, turning winds around the equinoxes and SSWs, are reflected in the observed c_{app}. Lower surface temperatures and stronger gradients in c_{eff} during winter explain the lower values of c_{app} with respect to summer.

[35] In conclusion, observations at I46RU deliver the proof for the existence of extremely small shadow zones, less than 100 km in size, for stratospheric arrivals. These results are applicable to a broad latitudinal range defined as the stratospheric surf zone, i.e., 20°N to 60°N where a rather stationary flow of stratospheric air occurs.

[36] **Acknowledgments.** The authors thank Peter Siegmund (KNMI) for discussions on the dynamics of the stratosphere. The suggestions of and discussions with David Green (AWE Blacknest, UK) are greatly appreciated. The CTBTO and station operators are thanked for guaranteeing the high quality of the IMS data and products. The work of J. T. Fricke is supported by the Netherlands Organization for Scientific Research (NWO). Figures in this article were made with the Generic Mapping Tools [*Wessel and Smith*, 1991].

References

Arnold, V. I. (2004), *Lectures on Partial Differential Equations*, 11–19 pp., Springer, Berlin.

Che, I., B. W. Stump, and H. Lee (2011), Experimental characterization of seasonal variations in infrasonic traveltimes on the Korean Peninsula with implications for infrasound event location, *Geophys. J. Int.*, *185*, 190–200.

Chunchuzov, I. P., S. N. Kulichkov, O. E. Popov, R. Waxler, and J. Assink (2011), Infrasound scattering from atmospheric anisotropic inhomogeneities, *Izv. Atmos. Oceanic Phys.*, *47*, 540–557.

Dahlman, O., S. Mykkeltveit, and H. Haak (2009), *Nuclear Test Ban: Converting Political Visions to Reality*, 83–97 pp., Springer, Dordrecht, Netherlands.

Donn, W. L., and D. Rind (1971), Natural infrasound as an atmospheric probe, *Geophys. J. R. Astron. Soc.*, *26*, 111–133.

Evers, L. G., and H. W. Haak (2007), Infrasonic forerunners: Exceptionally fast acoustic phases, *Geophys. Res. Lett.*, *34*, L10806, doi:10.1029/2007GL029353.

Evers, L. G., and P. Siegmund (2009), Infrasonic signature of the 2009 major sudden stratospheric warming, *Geophys. Res. Lett.*, *36*, L23808, doi:10.1029/2009GL041323.

Garcés, M. A., R. A. Hansen, and K. G. Lindquist (1998), Traveltimes for infrasonic waves propagating in a stratified atmosphere, *Geophys. J. Int.*, *135*, 255–263.

Green, D. N., and D. Bowers (2010), Estimating the detection capability of the International Monitoring System infrasound network, *J. Geophys. Res.*, *115*, D18116, doi:10.1029/2010JD014017.

Green, D. N., J. Vergoz, R. Gibson, A. Le Pichon, and L. Ceranna (2011), Infrasound radiated by the Gerdec and Chelopechene explosions: Propagation along unexpected paths, *Geophys. J. Int.*, *185*, 890–910.

Gutenberg, B. (1939), The velocity of sound waves and the temperature in the stratosphere above Southern California, *Bull. Am. Meteorol. Soc.*, *20*, 192–201.

Hedlin, M. A. H., D. Drob, K. Walker, and C. de Groot-Hedlin (2010), A study of acoustic propagation from a large bolide in the atmosphere with a dense seismic network, *J. Geophys. Res.*, *115*, B11312, doi:10.1029/2010JB007669.

Holton, J. R. (2004), *An Introduction to Dynamic Meteorology*, pp. 424–429, Elsevier Acad., Burlington, Mass.

Kulichkov, S. N., K. V. Avilov, G. A. Bush, O. E. Popov, O. M. Raspopov, A. K. Baryschnikov, D. O. ReVelle, and R. W. Whitaker (2004), On anomalously fast infrasonic arrivals at long distances from surface explosions, *Izv. Atmos. Oceanic Phys.*, *40*, 1–9.

Kulichkov, S. N., I. P. Chunchuzov, and O. I. Popov (2010), Simulating the influence of an atmospheric fine inhomogeneous structure on long range propagation of pulsed acoustic signals, *Izv. Atmos. Oceanic Phys.*, *46*, 69–77.

Le Pichon, A., J. Vergoz, E. Blanc, J. Guilbert, L. Ceranna, L. Evers, and N. Brachet (2009), Assessing the performance of the International Monitoring System's infrasound network: Geographical coverage and temporal variabilities, *J. Geophys. Res.*, *114*, D08112, doi:10.1029/2008JD010907.

Le Pichon, A., E. Blanc, and A. Hauchecorne (Eds.) (2010), *Infrasound Monitoring for Atmospheric Studies*, 629–646 pp., Springer, New York.

Mack, H., and E. A. Flinn (1971), Analysis of the spatial coherence of short-period acoustic-gravity waves in the atmosphere, *Geophys. J. R. Astron. Soc.*, *26*, 255–269.

McIntyre, M. E., and T. N. Palmer (1984), The 'surf zone' in the stratosphere, *J. Atmos. Terr. Phys.*, *46*, 825–849.

Melton, B. S., and L. F. Bailey (1957), Multiple signal correlators, *Geophysics*, *22*, 565–588.

Mentink, J., and L. G. Evers (2011), Frequency response and design parameters for differential microbarometers, *J. Acoust. Soc. Am.*, *130*, 33–41.

Plumb, R. A. (1996), A "tropical pipe" model of stratospheric transport, *J. Geophys. Res.*, *101*, 3957–3972.

ReVelle, D. O. (2010), Modified ray-mode (phase) theory: Understanding counter-wind propagation effects from atmospheric explosions, *J. Atmos. Solar Terr. Phys.*, *72*, 241–261.

Rind, D. H., and W. L. Donn (1978), Infrasound observations of variability during stratospheric warmings, *J. Atmos. Sci.*, *35*, 546–553.

Wessel, P., and W. H. F. Smith (1991), Free software helps map and display data, *Eos Trans. AGU*, *72*, 441.

L. G. Evers, J. T. Fricke, P. Smets, and A. R. J. van Geyt, Seismology Division, Royal Netherlands Meteorological Institute, PO Box 201, NL-3730 AE De Bilt, Netherlands. (evers@knmi.nl)